International Journal of Solids and Structures 325 (2026) 113727

Contents lists available at ScienceDirect

International Journal of Solids and Structures

journal homepage: www.elsevier.com/locate/ijsolstr

Dynamic fractures in rock-like materials analyzed by high-speed photography and a dynamic phase-field finite element model

P. Hesammokri *, S. Ershadrad, P. Isaksson

Solid Mechanics, The Ångström Laboratory, Uppsala University, SE-751 21 Uppsala, Sweden

ARTICLE INFO

Keywords:
Phase-field fracture theory
Dynamics
Mixed-mode fracture

ABSTRACT

A so-called hydrostatic-spectral-deviatoric decomposition is integrated into dynamic phase-field finite element models to study its effectiveness in the prediction of crack paths and crack tip velocities in brittle materials under dynamic mixed-mode compressive loading conditions. The study focuses on dynamic experiments, including drop tower tests conducted using gypsum plaster specimens with embedded flaws and holes. The hydrostatic-spectral-deviatoric decomposition method enables a split in tensile and compressive strain energy density contributions, crucial for capturing the complex fracture behavior in brittle materials under compressive loads that traditional models struggle to simulate effectively. Numerical simulations were conducted in parallel with experiments, utilizing a unified set of material parameters derived from prior work on the same material under quasi-static conditions. This approach ensured consistency between the dynamic and quasi-static cases. Numerical results demonstrated a good level of agreement with experiments, replicating key aspects of fracture evolution, including initiation and propagation of primary and secondary cracks as well as the temporal progression of crack tip velocities. This enhanced modeling approach offers a deeper understanding of dynamic fracture mechanisms in brittle materials and demonstrates its potential for advancing fracture simulations in applications involving dynamic, mixed-mode loading scenarios.

1. Introduction

Understanding and analyzing crack growth under dynamic conditions is critical across various scientific disciplines. In many real-world applications, materials are subjected to time-dependent loads—such as earthquakes, impact events, and blast loading—making it essential to account for dynamic effects when modeling fracture behavior. Foundational contributions in dynamic fracture mechanics, including the theoretical frameworks developed by Broberg (1989) and Freund and Freud (1998), and the high-speed experimental observations by Rosakis et al. (1999), have provided key insights into crack tip fields, energy flow, limiting crack speeds, and intersonic crack propagation. These studies helped guide the development of newer models that can better capture how cracks form and grow in complex situations. Among these, dynamic phase-field models have emerged as a powerful tool. Notably, works by Borden et al. (2012) and Hofacker and Miehe (2012) demonstrated their effectiveness in simulating complex fracture processes under high strain rates. These models have since been applied successfully across a wide range of materials and geometries, predicting crack paths, branching, and failure modes under dynamic loading conditions (Schlüter et al., 2016; Carollo et al., 2020; Mehrmashhadi et al., 2020; Mandal et al., 2020; Li et al., 2023; He et al., 2024; Yi et al., 2025).

Phase-field fracture models build upon the variational formulation of brittle fracture introduced by Francfort and Marigo (1998), and were regularized by Bourdin et al. (2000), extending the classical Griffith's theory of fracture. Dynamic extensions of this variational approach were later developed by Larsen (2010), laying the theoretical foundation for subsequent computational phase-field models. In many modern phase-field models, the strain energy density is typically decomposed into tensile (positive) and compressive (negative) components to accurately capture fracture behavior under different loading conditions. The positive component is assumed to drive material stiffness degradation (Ambati et al., 2015). Two widely used methods for decomposing strain energy density are the hydrostatic-deviatoric decomposition (Amor et al., 2009) and the spectral decomposition (Miehe et al., 2010b). However, these models encounter limitations when simulating fractures under shear and compressive loading conditions (Hesammokri et al., 2023). The spectral decomposition method struggles with shear scenarios, where material stiffness may remain despite the presence of a fully developed crack. Conversely, the hydrostatic-deviatoric decomposition method faces difficulties in mixed-mode compressive loading, often resulting in stiffness loss even upon crack closure.

* Corresponding author.
E-mail address: parnian.hesammokri@angstrom.uu.se (P. Hesammokri).

https://doi.org/10.1016/j.ijsolstr.2025.113727
Received 28 February 2025; Received in revised form 16 September 2025; Accepted 21 October 2025
Available online 28 October 2025

In the literature, phase-field models for compression-dominated fractures are predominantly utilized in rock mechanics. Zhang et al. (2017) introduced a modification to the spectral decomposition method for mixed-mode brittle fractures, proposing different critical energy release rates for various crack modes, based on a pioneering work by Shen and Stephansson (1994). Subsequent research has also explored similar modifications for mixed-mode fractures, cf. Spetz et al. (2020, 2021), Shajan et al. (2023). However, these modifications are not fully effective because they rely on spectral decomposition formulations that prevent material stiffness degradation, even when cracks are fully developed under pure shear loads. To address these limitations, a modification was proposed in Hesammokri et al. (2023). This modified strain energy density decomposition combines essential elements from both spectral and hydrostatic-deviatoric methods and incorporates a classical Mohr failure criterion. A key advantage of this approach is its ability to determine whether a compressive deformation field effectively drives the crack propagation process (e.g. crushing). The so-called hydrostatic-spectral-deviatoric decomposition was subsequently improved by integrating distinct critical energy release rates for different fracture modes (Hesammokri and Isaksson, 2024). This model has yielded promising results, replicating various crack paths and loading curves in diverse experimental conditions on brittle materials (Hesammokri et al., 2023; Hesammokri and Isaksson, 2024). However, its performance under dynamic loading scenarios is still uncertain.

In this study, the hydrostatic-spectral-deviatoric decomposition is integrated into dynamic finite element models to assess its effectiveness in predicting crack paths and crack tip velocities. This is achieved through dynamic experiments monitored using a high-speed camera, including drop tower tests using brittle gypsum plaster specimens with embedded flaws and holes. The comparison between numerical simulations and experimental data reveals a good agreement, showcasing the model's capability to provide meaningful insights into the complex fracture behavior of brittle materials.

2. Theory

Consider an isotropic linearly-elastic body, denoted Ω, Fig. 1, which includes an external boundary $\partial\Omega$ and a sharp crack Γ. A part of the boundary $\partial\Omega_{\boldsymbol{T}}$ is subject to prescribed traction $\boldsymbol{T}$, while $\partial\Omega_{\boldsymbol{u}}$ is subject to prescribed displacement $\boldsymbol{U}$. The total energy of the system can be formulated as

$$\Pi = \int_\Omega \Psi_k \mathrm{d}\boldsymbol{x} - \int_\Omega \Psi_e \mathrm{d}\boldsymbol{x} - \int_\Gamma G_c \mathrm{d}s, \tag{1}$$

where the term Ψ_k represents the kinetic energy density, Ψ_e is the strain energy density, G_c represents the critical energy release rate, and $\boldsymbol{x}$ denotes the spatial coordinates. A damage parameter d is introduced, $0 \leq d \leq 1$, so that a material point is intact when $d = 0$ and fully damaged when $d = 1$. The last term in (1) accounts for the energy used in creating new surfaces. Further, in a phase-field theory, the discrete crack Γ is approximated using a crack density function $\gamma(d, \nabla d)$, Fig. 1. This functional belongs to a family of elliptic functionals that approximate the Mumford-Shah functional (Braides, 1998). In this study, a crack density functional featuring linearity in d and quadratic dependence on ∇d, known as the AT1 model (Pham et al., 2011), is used. Unlike functionals with quadratic dependence on d (known as the AT2 model) that initiate damage evolution upon the application of load, resulting in the absence of a purely elastic response, the AT1 functional employed in this work maintains an elastic phase in the material until the point of fracture initiation (Suh et al., 2020; Geelen et al., 2019; Wu and Nguyen, 2018). The AT1 functional also promotes a more localized damage zone than the quadratic crack density functional AT2 (Bleyer and Alessi, 2018; Tanné et al., 2018). Using AT1, the last term in (1) is approximated as

$$\int_\Gamma G_c \mathrm{d}s \approx G_c \int_\Omega \gamma(d, \nabla d)\mathrm{d}\boldsymbol{x} = G_c \int_\Omega \frac{3}{8l}(d + l^2 \nabla d \cdot \nabla d)\mathrm{d}\boldsymbol{x}, \tag{2}$$

where l is a regularization parameter, controlling the width of the diffuse crack. The kinetic energy is

$$\int_\Omega \Psi_k \mathrm{d}\boldsymbol{x} = \frac{1}{2}\int_\Omega \rho \dot{\boldsymbol{u}} \cdot \dot{\boldsymbol{u}} \mathrm{d}\boldsymbol{x} \tag{3}$$

where $\dot{\boldsymbol{u}}$, and later occurring $\ddot{\boldsymbol{u}}$, denotes first and second derivatives of displacement $\boldsymbol{u}$ with respect to time t. The kinetic energy is unaffected by the crack phase-field d, but d locally degrades the stiffness of the material. Furthermore, in order to prevent crack growth in compression, the strain energy density is separated into two components: a positive portion Ψ_e^+ that is related to tensile strain and a negative portion Ψ_e^- that is related to compressive strain. In this study, these components are referred to as positive strain energy density and negative strain energy density, respectively, for clarity. It is assumed that only the positive component has an impact on the damage mechanism (stiffness degradation), cf. Ambati et al. (2015), i.e.,

$$\int_\Omega \Psi_e \mathrm{d}\boldsymbol{x} = \int_\Omega [(1-d)^2 \Psi_e^+ + \Psi_e^-]\mathrm{d}\boldsymbol{x}. \tag{4}$$

The Cauchy stress tensor $\boldsymbol{\sigma}$ and the consistent elastic stiffness tensor $\mathbf{C}$ are given by

$$\boldsymbol{\sigma} = (1-d)^2 \frac{\mathrm{d}\Psi_e^+}{\mathrm{d}\boldsymbol{\epsilon}} + \frac{\mathrm{d}\Psi_e^-}{\mathrm{d}\boldsymbol{\epsilon}}, \quad \text{and} \tag{5}$$

$$\mathbf{C} = (1-d)^2 \frac{\mathrm{d}^2\Psi_e^+}{\mathrm{d}\boldsymbol{\epsilon}^2} + \frac{\mathrm{d}^2\Psi_e^-}{\mathrm{d}\boldsymbol{\epsilon}^2}, \tag{6}$$

where $\boldsymbol{\epsilon} = \frac{1}{2}[\nabla\boldsymbol{u} + (\nabla\boldsymbol{u})^{\mathrm{T}}]$ is the linearized strain tensor. Now, using the above relations, the total energy in the body at time t is given by

$$\Pi = \int_\Omega [\frac{1}{2}\rho\dot{\boldsymbol{u}} \cdot \dot{\boldsymbol{u}} - (1-d)^2\Psi_e^+ - \Psi_e^- - \frac{3G_c}{8l}(d + l^2\nabla d \cdot \nabla d)]\mathrm{d}\boldsymbol{x}. \tag{7}$$

As noted in studies such as Shen and Stephansson (1994), Nejati et al. (2021), the critical energy release rates can vary significantly between different fracture modes in rock-like materials. For example, when a rock specimen with a single inclined flaw is subjected to compression, the fracture process unfolds in a distinct sequence: primary wing cracks form first, followed by secondary cracks, which are often interpreted as shear or mode II cracks. This sequential crack formation is driven by the notable difference in critical energy release rates for different fracture modes. Traditional criteria for critical energy release, such as those outlined in Shen and Stephansson (1994), have been found inadequate for capturing this phenomenon. Specifically, the critical energy release rate for an opening (mode I) crack, $G_{c\mathrm{I}}$, is often considerably lower than that for a shear (mode II) crack, $G_{c\mathrm{II}}$ (Li, 1986). To address this, Zhang et al. (2017) proposed separating the strain energy densities to account for the distinct critical energy release rates associated with mixed-mode I/II crack growth. In this study the method outlined by Zhang et al. (2017) is adapted to handle mode-dependent fracture toughness in brittle materials under mixed-mode compressive loading. The positive strain energy density, Ψ_e^+, is accordingly decomposed into two components, i.e.,

$$\Psi_e^+ = \Psi_{\mathrm{I}} + \Psi_{\mathrm{II}}, \tag{8}$$

where Ψ_{I} is associated with mode I fracture and Ψ_{II} is associated with mode II fracture. Introducing $G_{c\mathrm{I}}$ and $G_{c\mathrm{II}}$, the ratio Ψ_e^+/G_c is written as (Zhang et al., 2017)

$$\frac{\Psi_e^+}{G_c} = \frac{\Psi_{\mathrm{I}}}{G_{c\mathrm{I}}} + \frac{\Psi_{\mathrm{II}}}{G_{c\mathrm{II}}}. \tag{9}$$

Further, to establish irreversible crack growth in computer simulations, a history field $\mathcal{H}$ is defined using (9), i.e.,

$$\mathcal{H}(\boldsymbol{u}, t) = \max_{\tau\in[0,t]} \{ \frac{\Psi_{\mathrm{I}}}{G_{c\mathrm{I}}} + \frac{\Psi_{\mathrm{II}}}{G_{c\mathrm{II}}} \}, \tag{10}$$

The presence of the history field $\mathcal{H}$ ensures that the highest strain energy density experienced during the loading history of the material

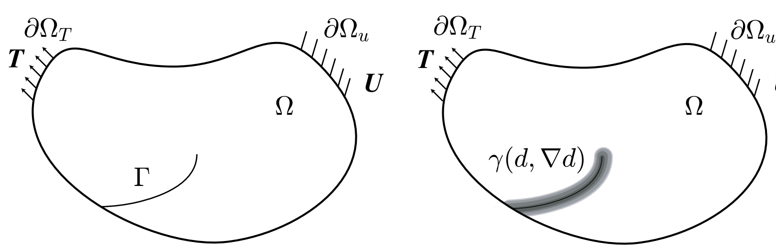

Fig. 1. Discrete vs diffusive crack representation.

determines its current damage state, preventing any possibility of healing (Miehe et al., 2010b). It is important to note that stresses are still reversible and their evaluation follows (5). Variation of the functional in (7) gives the governing equations in the strong form, neglecting any body forces,

$$\begin{cases} \nabla \cdot \boldsymbol{\sigma} = \rho \ddot{\boldsymbol{u}} & \text{on } \Omega, \\ (1-d)\mathcal{H} - \frac{3}{16l} - \frac{3l}{8}\nabla^2 d = 0. & \text{in } \Omega, \\ \boldsymbol{u} = \boldsymbol{U} & \text{on } \partial\Omega_u, \\ \boldsymbol{\sigma} \cdot \boldsymbol{n} = \boldsymbol{T} & \text{on } \partial\Omega_T, \\ \nabla d \cdot \boldsymbol{n} = 0 & \text{on } \partial\Omega, \end{cases} \tag{11}$$

where $\boldsymbol{n}$ denotes the normal to the boundary $\partial\Omega$.

2.1. Strain energy density decomposition

In order to simulate mixed-mode fracture under compressive loading, the hydrostatic-spectral-deviatoric decomposition is utilized (Hesammokri et al., 2023; Hesammokri and Isaksson, 2024). This method combines aspects of both the spectral (Miehe et al., 2010a) and the hydrostatic-deviatoric (Amor et al., 2009) decompositions along with a classical Mohr failure criterion. In the spectral decomposition, the strain energy density is written in terms of principal strains ϵ_1, ϵ_2, and ϵ_3 and then decomposed into tensile (positive) and compressive (negative) components: $\Psi_e^{\pm} = \frac{1}{2}\lambda \langle \epsilon_1 + \epsilon_2 + \epsilon_3 \rangle_{\pm}^2 + \mu \langle \epsilon_1 \rangle_{\pm}^2 + \mu \langle \epsilon_2 \rangle_{\pm}^2 + \mu \langle \epsilon_3 \rangle_{\pm}^2$, where μ and λ are Lamé parameters. $\langle \cdot \rangle_+$ and $\langle \cdot \rangle_-$ select the positive and negative parts of their argument, i.e. $\langle x \rangle_+ = x$, if $x \geq 0$; 0 if $x < 0$, and $\langle x \rangle_- = x$, if $x \leq 0$; 0 if $x > 0$. In the hydrostatic-deviatoric decomposition, the strain energy density is expressed as the sum of hydrostatic and deviatoric components: $\Psi_e = \frac{1}{2}K(\mathrm{tr}\,\boldsymbol{\epsilon})^2 + \mu\,\mathrm{tr}(\mathbf{e}^2)$, where K is the bulk modulus and $\mathbf{e} = \boldsymbol{\epsilon} - \mathrm{tr}\boldsymbol{\epsilon}/m$ is the deviatoric strain in which m is the number of spatial dimensions. The hydrostatic component is further divided into tensile(positive) and compressive (negative) parts, while the deviatoric component remains undecomposed: $\Psi_e^+ = \frac{1}{2}K \langle \mathrm{tr}\,\boldsymbol{\epsilon} \rangle_+^2 + \mu\,\mathrm{tr}\left(\mathbf{e}^2\right)$, and $\Psi_e^- = \frac{1}{2}K \langle \mathrm{tr}\,\boldsymbol{\epsilon} \rangle_-^2$ (for more details regarding both decomposition strategies see Miehe et al. (2010b), Amor et al. (2009), Hesammokri et al. (2023), Hesammokri and Isaksson (2024)).

The primary motivation of employing a hydrostatic-spectral-deviatoric decomposition is to account for the influence of compressive strains on crack growth. Starting from the hydrostatic-deviatoric decomposition, the deviatoric term $\Psi_{\mathrm{dev}} = \mu\,\mathrm{tr}(\mathbf{e}^2)$ is further divided into tensile Ψ_{dev}^+ and compressive Ψ_{dev}^- components through a spectral decomposition. This is achieved by writing Ψ_{dev} in terms of principal strains: $\Psi_{\mathrm{dev}} = \mu\frac{m-1}{m}(\epsilon_1^2+\epsilon_2^2+\epsilon_3^2) - \mu\frac{2}{m}(\epsilon_1\epsilon_2 + \epsilon_1\epsilon_3 + \epsilon_2\epsilon_3)$. The final formulation for the hydrostatic-spectral-deviatoric decomposition is

$$\Psi_e^+ = \frac{1}{2}K \langle \mathrm{tr}\,\boldsymbol{\epsilon} \rangle_+^2 + \Psi_{\mathrm{dev}}^+ + \phi\Psi_{\mathrm{dev}}^-, \quad \Psi_e^- = \frac{1}{2}K \langle \mathrm{tr}\,\boldsymbol{\epsilon} \rangle_-^2 + (1-\phi)\Psi_{\mathrm{dev}}^-, \tag{12}$$

where Ψ_{dev}^+ and Ψ_{dev}^- are formulated as

$$\begin{aligned} \Psi_{\mathrm{dev}}^+ = \mu\tfrac{m-1}{m}[\langle\epsilon_1\rangle_+^2 + \langle\epsilon_2\rangle_+^2 + \langle\epsilon_3\rangle_+^2] - \mu\tfrac{2}{m}[&\langle\epsilon_1\rangle_+\langle\epsilon_2\rangle_- + \langle\epsilon_2\rangle_+\langle\epsilon_1\rangle_- + \\ &\langle\epsilon_1\rangle_+\langle\epsilon_3\rangle_- + \langle\epsilon_3\rangle_+\langle\epsilon_1\rangle_- + \langle\epsilon_3\rangle_+\langle\epsilon_2\rangle_- + \langle\epsilon_2\rangle_+\langle\epsilon_3\rangle_-], \quad \text{and} \\ \Psi_{\mathrm{dev}}^- = \mu\tfrac{m-1}{m}&[\langle\epsilon_1\rangle_-^2 + \langle\epsilon_2\rangle_-^2 + \langle\epsilon_3\rangle_-^2]. \end{aligned}$$

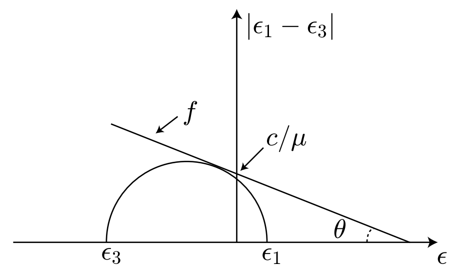

Fig. 2. Mohr diagram and failure envelope.

(13)

The variable ϕ can take the value 0 or 1 based on a Mohr failure criterion (Labuz and Zang, 2012) and controls whether or not Ψ_{dev}^- contributes to crack growth (crushing). The criterion is based on a fracture surface defined as (sorting $\epsilon_1 \geq \epsilon_2 \geq \epsilon_3$)

$$f = \frac{\lambda+\mu}{\mu}\frac{\epsilon_1+\epsilon_3}{\epsilon_1-\epsilon_3}\sin\theta - \frac{c}{\mu(\epsilon_1-\epsilon_3)}\cos\theta + 1\,. \tag{14}$$

In (12), $\phi = 1$ if $f \geq 0$, otherwise $\phi = 0$. The variable c represents an inherent cohesive stress, while θ represents an angle of internal friction as depicted in Fig. 2. The associated mode I and mode II contributions to the positive strain energy density for spectral, hydrostatic-deviatoric (hyd-dev), and hydrostatic-spectral-deviatoric (hyd-spect-dev) decompositions are assumed as (Hesammokri and Isaksson, 2024)

$$\begin{aligned} \Psi_{\mathrm{I}} &= \begin{cases} \frac{1}{2}\lambda\langle\epsilon_1+\epsilon_2+\epsilon_3\rangle_+^2 & \text{spectral}, \\ \frac{1}{2}K\langle\mathrm{tr}\,\boldsymbol{\epsilon}\rangle_+^2 & \text{hyd-dev}, \\ \frac{1}{2}K\langle\mathrm{tr}\,\boldsymbol{\epsilon}\rangle_+^2 & \text{hyd-spect-dev}, \end{cases} \\ \Psi_{\mathrm{II}} &= \begin{cases} \mu\left(\langle\epsilon_1\rangle_+^2 + \langle\epsilon_2\rangle_+^2 + \langle\epsilon_3\rangle_+^2\right) & \text{sepectral}, \\ \mu\,\mathrm{tr}\left(\mathbf{e}^2\right) & \text{hyd-dev}, \\ \Psi_{\mathrm{dev}}^+ + \phi\Psi_{\mathrm{dev}}^- & \text{hyd-spect-dev}. \end{cases} \end{aligned} \tag{15}$$

In Appendix B are examples of fracture stress surfaces in tension and compression, i.e., stress combinations to nucleate damage, displayed to further contrast the three decomposition strategies.

2.2. Spatial discretization

The derivation of the weak form for the governing equation of the crack phase-field problem has been extensively detailed in various works, including Nguyen et al. (2015). To obtain the weak form, the second equation in Eq. (11) is multiplied by an arbitrary test function, δd, and then integrated over the domain Ω, giving

$$\int_\Omega \left(2\mathcal{H}d\delta d + \frac{3G_c l}{4}\nabla d\nabla(\delta d)\right)\mathrm{d}\boldsymbol{x} = \int_\Omega \left(2\mathcal{H} - \frac{3G_c}{8l}\right)\delta d\,\mathrm{d}\boldsymbol{x}. \tag{16}$$

Discretizing, such that $d(\boldsymbol{x}) = \mathbf{N}(\boldsymbol{x})\mathbf{d}_i$, $\nabla d(\boldsymbol{x}) = \mathbf{B}(\boldsymbol{x})\mathbf{d}_i$, $\delta d(\boldsymbol{x}) = \mathbf{N}(\boldsymbol{x})\delta\mathbf{d}_i$ and $\nabla\delta d(\boldsymbol{x}) = \mathbf{B}(\boldsymbol{x})\delta\mathbf{d}_i$ where $\mathbf{d}_i$ are the nodal values of the crack phase-field d and $\mathbf{N}$ and $\mathbf{B} = \delta\mathbf{N}/\delta\boldsymbol{x}$ are standard finite element basis functions and their first spatial derivatives. Observing that the test function is arbitrary, we get the discretized equation for the crack phase-field as

$$\mathbf{K}_d\mathbf{d}_i = \mathbf{f}_d, \tag{17}$$

where

$$\mathbf{K_d} = \int_\Omega \left(\mathcal{H}\mathbf{N}^{\mathrm{T}}\mathbf{N} + \frac{3G_c l}{8}\mathbf{B}^{\mathrm{T}}\mathbf{B}\right)\mathrm{d}\boldsymbol{x}, \tag{18}$$

and

$$\mathbf{f}_d = \int_\Omega \left(\mathcal{H} - \frac{3G_c l}{16 l}\right)\mathbf{N}^{\mathrm{T}}\mathrm{d}\boldsymbol{x}. \tag{19}$$

For the displacement problem, the weak form of the governing equations is obtained by multiplying the first equation in Eq. (11) with an arbitrary test function $\delta\boldsymbol{u}$ and integration over the domain Ω. Using Eqs. (5)–(6) the weak form is

$$\int_\Omega \left((\nabla\delta\boldsymbol{u})^{\mathrm{T}}((1-d)^2\mathbf{C}^+ + \mathbf{C}^-)\nabla\boldsymbol{u} + \delta\boldsymbol{u}\rho\ddot{\boldsymbol{u}}\right)\mathrm{d}\boldsymbol{x} = \int_{\partial\Omega_T} \delta\boldsymbol{u}\boldsymbol{T}\mathrm{d}(\partial\Omega_T) \tag{20}$$

where

$$\mathbf{C}^+ = \frac{\mathrm{d}^2\Psi_e^+}{\mathrm{d}\epsilon^2}, \quad \text{and} \quad \mathbf{C}^- = \frac{\mathrm{d}^2\Psi_e^-}{\mathrm{d}\epsilon^2}. \tag{21}$$

Discretizing, such that $\boldsymbol{u}(\boldsymbol{x}) = \mathbf{N}(\boldsymbol{x})\mathbf{u}_i$, $\nabla\boldsymbol{u}(\boldsymbol{x}) = \mathbf{B}(\boldsymbol{x})\mathbf{u}_i$, $\delta\boldsymbol{u}(\boldsymbol{x}) = \mathbf{N}(\boldsymbol{x})\delta\mathbf{u}_i$ and $\nabla\delta\boldsymbol{u}(\boldsymbol{x}) = \mathbf{B}(\boldsymbol{x})\delta\mathbf{u}_i$ where $\mathbf{u}_i$ are the nodal values of the displacement field $\boldsymbol{u}$, and again observing that the test function is arbitrary, the stiffness matrix for the displacement problem is given by

$$\mathbf{K}_{\boldsymbol{u}} = \int_\Omega \mathbf{B}^{\mathrm{T}}((1-d)^2\mathbf{C}^+ + \mathbf{C}^-)\mathbf{B}\mathrm{d}\boldsymbol{x}, \tag{22}$$

while the external force vector is given by

$$\mathbf{F} = \int_{\partial\Omega T} \mathbf{N}^{\mathrm{T}}\boldsymbol{T}\mathrm{d}(\partial\Omega_T). \tag{23}$$

Finally, the discretized dynamic equation for the displacement field is formulated as (neglecting any internal damping)

$$\mathbf{M}\ddot{\mathbf{u}}_i + \mathbf{K}_{\boldsymbol{u}}\mathbf{u}_i = \mathbf{F}, \tag{24}$$

where $\mathbf{M}$ is the mass matrix.

2.3. Time integration

The dynamic displacement problem is solved in a staggered manner using the Newmark time integration scheme (Newmark, 1959). At each time step, Eq. (24) is solved using

$$\mathbf{M}\ddot{\boldsymbol{u}}_{k+1} + \mathbf{K}_{\boldsymbol{u}}(\bar{\boldsymbol{u}}_{k+1} + \frac{1}{2}\ddot{\boldsymbol{u}}_{k+1}\beta_2\Delta t^2) = \mathbf{F}_{k+1}, \tag{25}$$

where $\Delta t = t_{k+1} - t_k$ is the incremental time step. Initially, the displacement and velocity fields for step $k+1$ are predicted using solutions from the previous time step k,

$$\begin{aligned}\bar{\boldsymbol{u}}_{k+1} &= \boldsymbol{u}_k + \dot{\boldsymbol{u}}_k\Delta t + \frac{1}{2}\ddot{\boldsymbol{u}}_k(1-\beta_2)\Delta t^2 \\ \dot{\bar{\mathbf{u}}}_{k+1} &= \dot{\boldsymbol{u}}_k + \ddot{\boldsymbol{u}}_k(1-\beta_1)\Delta t.\end{aligned} \tag{26}$$

The predicted fields are then applied to solve the dynamics, Eq. (25), giving the acceleration of the next time step, i.e.,

$$\ddot{\boldsymbol{u}}_{k+1} = \left(\mathbf{M} + \frac{1}{2}\mathbf{K}_{\boldsymbol{u}}\beta_2\Delta t^2\right)^{-1}\left(\mathbf{F}_{k+1} - \mathbf{K}_{\boldsymbol{u}}\bar{\boldsymbol{u}}_{k+1}\right). \tag{27}$$

The corrected displacement and velocity fields are then obtained,

$$\begin{aligned}\boldsymbol{u}_{k+1} &= \bar{\boldsymbol{u}}_{k+1} + \frac{1}{2}\ddot{\boldsymbol{u}}_{k+1}\beta_2\Delta t^2 \\ \dot{\boldsymbol{u}}_{k+1} &= \dot{\bar{\mathbf{u}}}_{k+1} + \ddot{\boldsymbol{u}}_{k+1}\beta_1\Delta t.\end{aligned} \tag{28}$$

The crack phase problem is independently solved based on the displacement field $\boldsymbol{u}_{k+1}$. Throughout this study, a fully explicit Newmark algorithm is used, with constants $\beta_1 = 1/2$ and $\beta_2 = 0$, and, for simplicity, a lumped mass matrix $\mathbf{M}$ (i.e., a diagonal mass matrix) is employed and vanishing external forces (i.e., $\mathbf{F} = 0$).

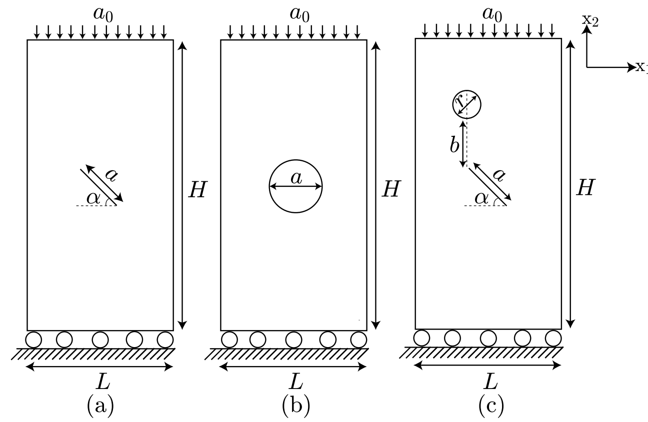

Fig. 3. Load and geometries: Inclined notch (a), single-hole (b), and inclined notch with one hole (c).

3. Experiments

In order to validate the hydrostatic-spectral-deviatoric decomposition, drop tower tests were conducted. Schematics of sample geometries and their loading conditions are shown in Fig. 3. The geometries are: a geometry with an inclined notch, a geometry with a single hole, and a geometry with a hole and an inclined notch (Fig. 3). The dimensions are: $H = 100$ mm, $L = 50$ mm, $a = 20$ mm, $b = 15$ mm, $r = 10$ mm, and $\alpha = 45°$. The experimental specimens were prepared by casting a mixture of gypsum plaster and water into molds, resulting in specimen thicknesses of 10 mm. All batches were mixed using the same proportions of gypsum plaster and water (for our particular gypsum, this equated to a precise combination of two parts gypsum plaster to one part water by mass). The samples were taken out from the molds after three hours and baked in an oven for 90 min in 180 °C in order to make them dry and brittle. The samples were tested using a drop tower rig equipped with a 2.4 kg drop weight (see Fig. 4). The weight was dropped on the samples from various heights (the drop height, denoted as h_{drop}, is illustrated in Fig. 4). It should be mentioned that the inclined notches were introduced with relatively wide openings to ensure that the opposing faces would not come into contact during loading. The crack propagation process was monitored during all tests using a MotionPro Y series high-speed camera capable of capturing up to 70,000 frames per second. The velocity variation of the specimen's upper edge during impact was analyzed using the high-speed camera by tracking the displacement of the dropping weight before and after impact and recording its position over time for different drop heights (see Fig. 5). The dropping weight remains in contact with the specimen's upper edge after impact until all cracks in the specimen are fully developed. As shown in Fig. 5, the displacement follows a linear trend after impact, indicating that the velocity remained nearly constant during impact. The velocity during impact v_0 was determined by fitting (straight) lines to the experimentally estimated displacement data for different drop heights.

4. Numerical simulations

In the numerical simulations, the impact event was modeled by applying an initial acceleration to the specimen's top boundary, allowing its velocity to evolve naturally. The bottom boundary was constrained in the vertical direction, while the vertical boundaries remained stress-free (see Fig. 3). In the simulations, no constraints were applied in the horizontal direction; the specimen was allowed to move freely, consistent with the experimental setup in which the specimen was placed on a surface without lateral confinement. Since no contact between notch faces was observed in the experiments, contact conditions were

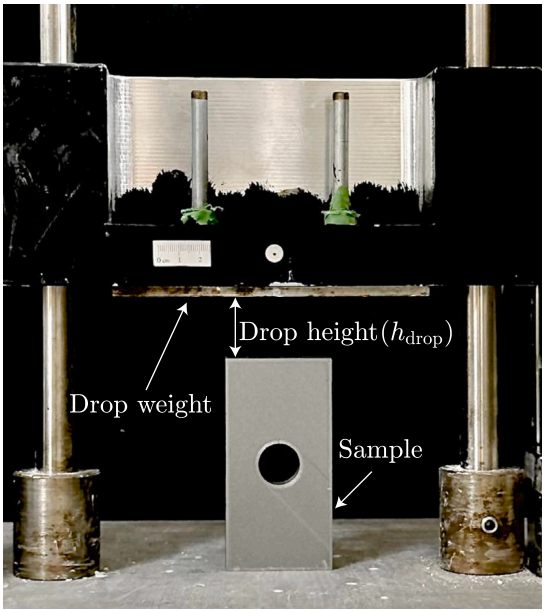

Fig. 4. Drop tower machine.

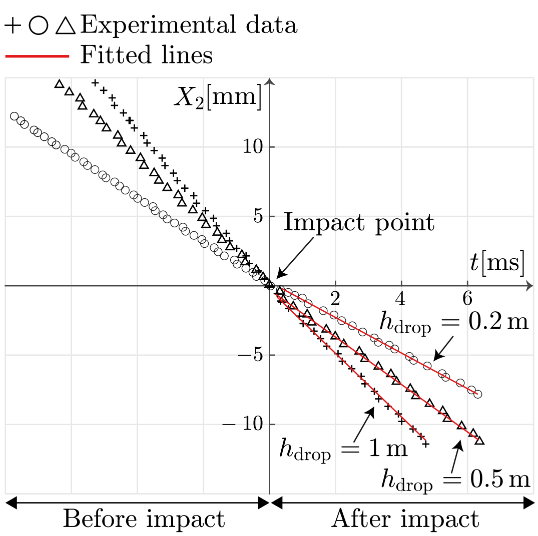

Fig. 5. Displacement of the dropping weight over time before and after impact for different drop heights, along with their fitted linear trends: for $h_{drop} = 0.2$m, $v_0 = \mathrm{d}X_2/\mathrm{d}t = -1.23$ m/s; for $h_{drop} = 0.5$m, $v_0 = \mathrm{d}X_2/\mathrm{d}t = -1.72$ m/s; and for $h_{drop} = 1$ m, $v_0 = \mathrm{d}X_2/\mathrm{d}t = -2.36$ m/s.

not included in the numerical models for geometries having inclined notches. The initial acceleration of the top boundary in the vertical direction was given as $a_0 = -v_0/t_0$, where $t_0 = 0.1\,\mu$s represents the impulse duration. For $t > t_0$ the acceleration of the top boundary where held at zero, meaning that its velocity in the vertical direction remained constant at $-v_0$ after impact, in agreement with experimental observations (see Fig. 5). This approach ensures that the specimen's motion is governed by the dynamic response of the system, providing a physically sound representation of the impact event.

All material parameters, including the regularization length l, were directly adopted from Hesammokri and Isaksson (2024), which focused on the same material under quasi-static loading conditions. This ensured that the simulations were performed with a unified set of material parameters, maintaining consistency between the dynamic and quasi-static cases without the need for recalibration. The parameters are as follows: Young's modulus $E = 650\,$MPa, Poisson's ratio $\nu = 0.2$, cohesive strength $c = 21\,$MPa, critical energy release rate for mode I $G_{cI} = 9.1\,$N/m, critical energy release rate for mode II $G_{cII} = 130\,$N/m, internal friction angle $\theta = \pi/6$, and density $\rho = 1230\,\mathrm{kg/m^3}$. In phase-field models, the regularization length l is a critical parameter as it governs the width of the diffuse crack zone and strongly influences the fracture behavior. To maintain consistency with the material parameters from the quasi-static study (Hesammokri and Isaksson, 2024), a constant $l = 504\,\mu$m was selected. Moreover, in all meshes $h \leq l/2$ where h represents the maximum element edge length in each mesh. It should be mentioned that to resolve the fracture process zone with sufficient accuracy, a structured, non-adaptive mesh was employed. Although the mesh remains fixed during the simulation, finer elements were placed in critical regions such as in the vicinities of cracks, notches and holes. The mesh resolution was selected to satisfy the commonly accepted condition for AT1, $h \leq l/2$, which provides an adequate balance between computational efficiency and the accurate capture of key features in the dynamic simulations. Fixing l ensured a consistent framework for both quasi-static and dynamic simulations, preserving the integrity and comparability of the material model across different loading conditions. All equations were solved using established finite element algorithms implemented in a Matlab (MATLAB, 2024) code. A flowchart illustrating the adopted scheme is provided in Fig. 6. In the computations, standard bi-linear 4-node isoparametric elements were employed, assuming plane strain conditions. Although the specimen's thickness is indeed relatively small compared to the other dimensions of the specimen, the plane strain condition was selected because the specimen's thickness is big enough to confine the specimen in the thickness direction. Hence, the fracture process and deformation are primarily two-dimensional within the plane of the specimen (Carlsson and Isaksson, 2018, 2019; Hesammokri et al., 2023; Hesammokri and Isaksson, 2024; Spetz et al., 2021, 2020). With plane strain assumption the Lamé coefficients are given by: $\mu = E/[2(1+\nu)]$ and $\lambda = E\nu/[(1+\nu)(1-2\nu)]$. In all simulations a constant time step $\Delta t = 0.1\,\mu$s was used, which is well below the traditional upper limit h_{min}/c_0, where h_{min} is the smallest element length in the mesh and $c_0 = \sqrt{E/\rho}$ is the material's theoretical pressure wave speed. Finally, the dynamic model is evaluated (benchmarked) in Appendix A, where the hydrostatic-spectral-deviatoric decomposition is used in simulations of two well-known and widely adopted dynamic crack growth cases.

5. Results and discussion

Dynamic compression experiments in different heights were performed for the sample geometries and the resulting crack patterns for each case are compared to the experiments (Figs. 7, 10, and 12).

5.1. Inclined notch

The results of the inclined notch test, as depicted in Fig. 7, provide a comparison in crack paths between the numerical simulations and experiments for three different drop heights. The experiments reveal a consistent pattern in crack formation across different drop heights, with both primary and secondary cracks identifiable. The primary cracks, indicated by black arrows, align with the expected paths predicted by the simulation. This alignment across all tested heights (0.2 m, 0.5 m, and 1 m) is observed. By examining the distribution of the first principal strain and the volumetric strain at the tip of the primary cracks, it is illustrated that these cracks are primarily driven by tensile strains, as illustrated in Fig. 8. Following the emergence of the primary cracks, secondary cracks begin to propagate horizontally, as indicated by the red arrows. The secondary cracks are wide indicating that substantial amount of crushing are taking place. This behavior is also captured in the simulation results, which mirror the experimental observations. An analysis of the strain fields at the tips of the secondary cracks (see

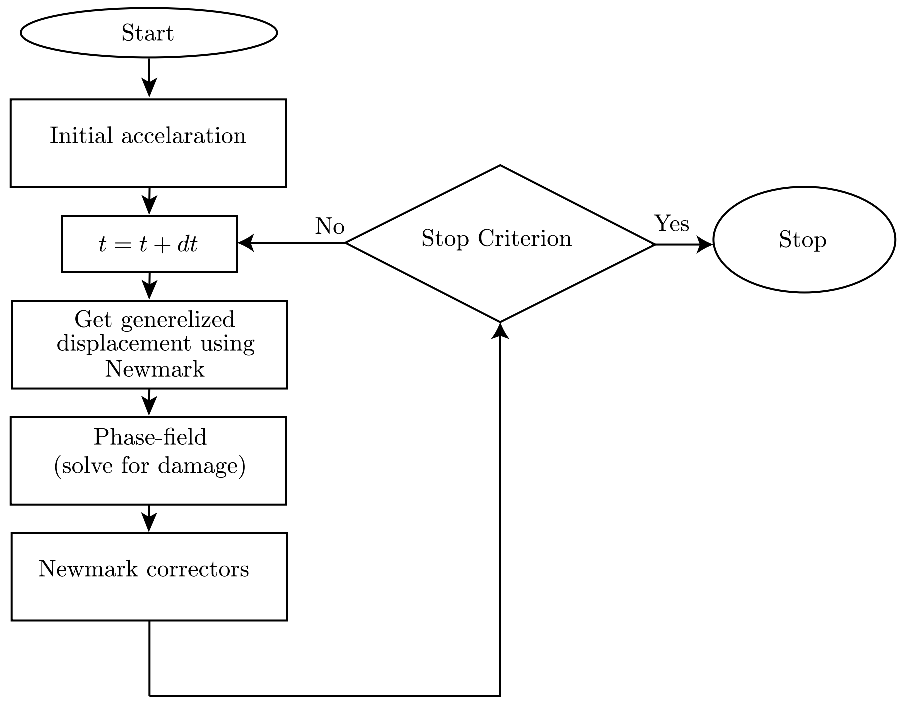

Fig. 6. Flowchart of the scheme used in the simulations.

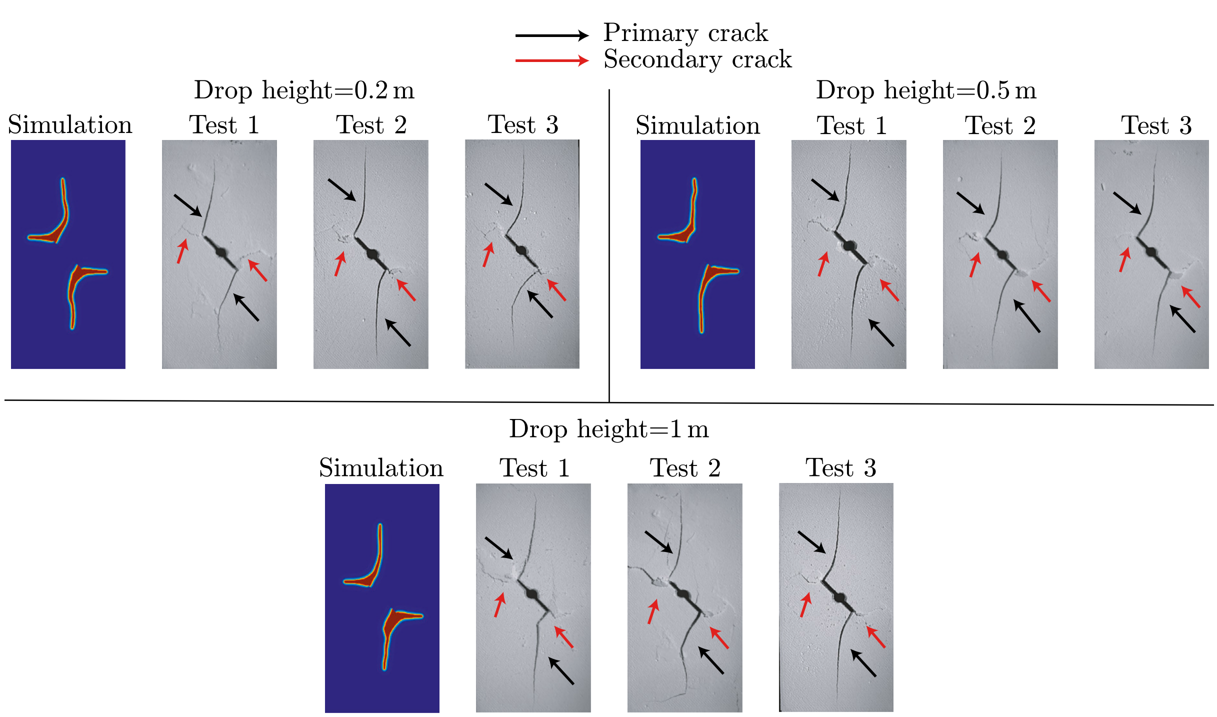

Fig. 7. Inclined notch: Crack paths for simulations and experiments for different heights.

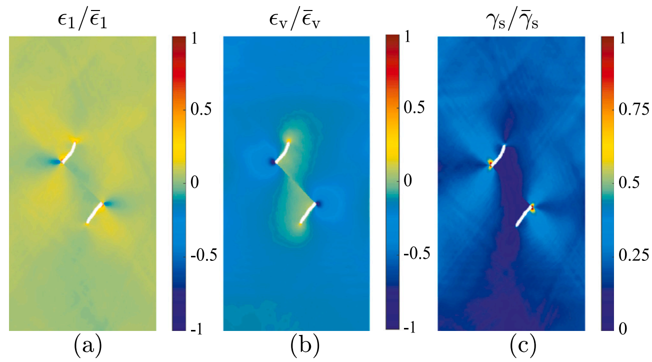

Fig. 8. Inclined notch simulation: Distributions of first principal strain ϵ_1 (a), volumetric strain ϵ_v (b), and principal shear strain γ_s (c). The strain fields are normalized by their highest values, $\bar{\epsilon}_1$, $\bar{\epsilon}_v$ and $\bar{\gamma}_s$, respectively.

Fig. 8) indicates that these cracks propagate under compressive conditions, which implies crushing. Notably, the secondary cracks are driven principally by deviatoric strains, dictated by the Mohr criterion (14). The simulations were terminated based on a stop criterion once the cracks had propagated sufficiently to allow for meaningful comparisons with the experimental results. Specifically, for the inclined notch test, all simulations were halted when the crack extended to 1/2 of the horizontal distance between the initial crack tip and the boundary.

To evaluate the model's accuracy, we compared the primary crack tip velocity v_c (Fig. 9a) estimated from an experiment conducted at a drop height of 5 cm with the simulation results, as shown in Fig. 9. The crack tip position was tracked using a high-speed camera, and the mean velocity for each frame was calculated (represented by the cross marks in Fig. 9b). The camera operated at a maximum speed of 70,000 frames per second to ensure accurate tracking of the crack tip position. Due to the technical limitations of the high-speed camera, particularly its frame rate, obtaining a larger number of experimental data points was not possible. Nevertheless, the data collected captured the general trend of the crack tip velocity. As shown in Fig. 9, the hydrostatic-spectral-deviatoric decomposition model reproduced the overall experimental trend, including the deceleration and subsequent stabilization of the crack tip velocity. This is further illustrated by the crack field progression at different times (Fig. 9b), where extensive crack growth is visible in the early stage, followed by steady slower growth in later stages.

5.2. Single-hole

The results of the single-hole tests, as shown in Fig. 10, shows a comparison between numerical simulations and experimental observations at three different drop heights. Across all drop heights, a consistent pattern of crack formation is observed, with both primary and secondary cracks identifiable. The primary cracks, indicated by black arrows, propagate vertically from the top and bottom of the hole, closely aligning with the predicted paths in the simulations. This alignment is consistent across all tested heights. Secondary cracks, indicated by red arrows, emerge on the far left and far right sides of the hole. One may notice in the experimental observations that the secondary cracks are quite wide, blunt, indicating that substantial amount of crushing are taking place. By analyzing the strain distribution near the crack tips (Fig. 11), it is confirmed that the primary cracks are predominantly driven by tensile strains, while the secondary cracks predominantly develop under compression, indicating crushing, influenced by deviatoric strains as dictated by the Mohr criterion (14), as shown in Fig. 11. Notably, the secondary cracks propagate much more rapidly as the drop height increases. For instance, at a drop height of 0.2 m, the primary cracks extended throughout the specimen, closely reaching the edges before secondary cracks began to form. However, in the other two cases, this process occurred significantly faster. As the impact energy increases with the drop height, the critical level defined by the Mohr criterion (14) is reached more quickly, leading to the earlier initiation of secondary crack formation. Overall, the numerical simulations demonstrate good agreement with the experimental results, effectively capturing the complex fracture behavior observed in the tests. All simulations for the single-hole test were terminated once a crack had grown to 1/3 of the horizontal distance between the initial crack tip and the boundary.

5.3. Comparison of hydrostatic-deviatoric, spectral, and hydrostatic-spectral-deviatoric decompositions

Another intriguing avenue for investigation is comparing the crack paths generated by the hydrostatic-spectral-deviatoric decomposition with those produced by the hydrostatic-deviatoric decomposition (Amor et al., 2009) and the spectral decomposition (Miehe et al., 2010a). Such a comparison has already been conducted under quasi-static conditions (Hesammokri and Isaksson, 2024), where it was demonstrated that, for complex specimen geometries, the hydrostatic-spectral-deviatoric decomposition outperformed the other two methods, reproducing all the intriguing experimental crack patterns. In contrast, the hydrostatic-deviatoric and spectral decompositions failed to replicate the observed experimental behavior. To further evaluate the model's performance relative to these decompositions for dynamic cases, crack patterns were analyzed for a 'non-symmetric' case (see Fig. 3c), and experiments and simulations were performed for a drop height of 0.2 m. The results demonstrate a distinct sequence of crack development, as shown in Fig. 12. Initially, consistent with the behavior observed in the inclined notch test, primary cracks formed at the initial tips of the notch. Subsequently, secondary cracks emerged at the upper and lower edges of the hole. In the next phase, horizontal cracks (tertiary cracks) began to propagate from the notch's initial tips. Similar to the results for the previous specimens, the developed horizontal cracks are wide, blunt, indicating substantial amount of crushing. All these cracks were accurately captured and simulated using the hydrostatic-spectral-deviatoric decomposition (Fig. 12). Based on the earlier discussion and the strain distributions illustrated in Figs. 8 and 11, it is illustrated that the primary and secondary cracks predominantly grow under tension and the tertiary cracks primarily propagate under compression. Compared to the hydrostatic-spectral-deviatoric decomposition, the hydrostatic-deviatoric and spectral decompositions did not fully capture all crack paths. With the hydrostatic-deviatoric decomposition, the primary cracks formed first, followed by the simultaneous development of tertiary cracks and only one of the secondary cracks (originating from the lower part of the hole), which did not fully develop. As a result, this decomposition did not accurately capture all the crack paths and also deviated from the expected sequence of crack formation. The spectral decomposition identified only the primary and secondary cracks, while the tertiary cracks were not nucleated. For the hydrostatic-spectral-deviatoric and hydrostatic-deviatoric decompositions, the simulations stopped once a crack had propagated to 1/3 of the horizontal distance between the initial notch tip and the boundary, and for the spectral decomposition, the termination criterion was reached when a crack extended to 2/3 of the vertical distance between an initial notch tip and the boundary.

5.4. Discussion

Based on the presented results, the hydrostatic-spectral-deviatoric decomposition demonstrates a potential to replicate complex dynamic crack paths and the sequence of several evolving cracks using a unified set of material parameters consistent with quasi-static cases. However, when comparing experimental and simulation outcomes, some minor differences in crack paths are observed. These discrepancies can be largely attributed to the complex and heterogeneous nature of the

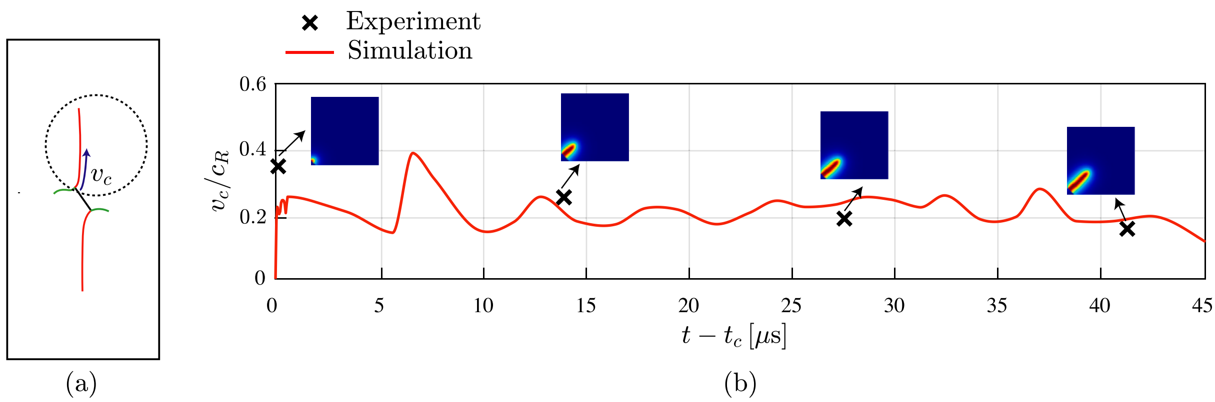

Fig. 9. Crack tip velocity: Schematic of the selected region used for analyzing the crack tip velocity (a), a comparison of the variation in crack tip velocity v_c normalized by Rayleigh wave speed c_R between the experiment and simulation, along with the zoomed crack field progression at different time points (b). $t = t_c$ is the onset of crack formation. For the used material c_R is calculated as 426.23 m/s, and v_0 is set to −0.54 m/s.

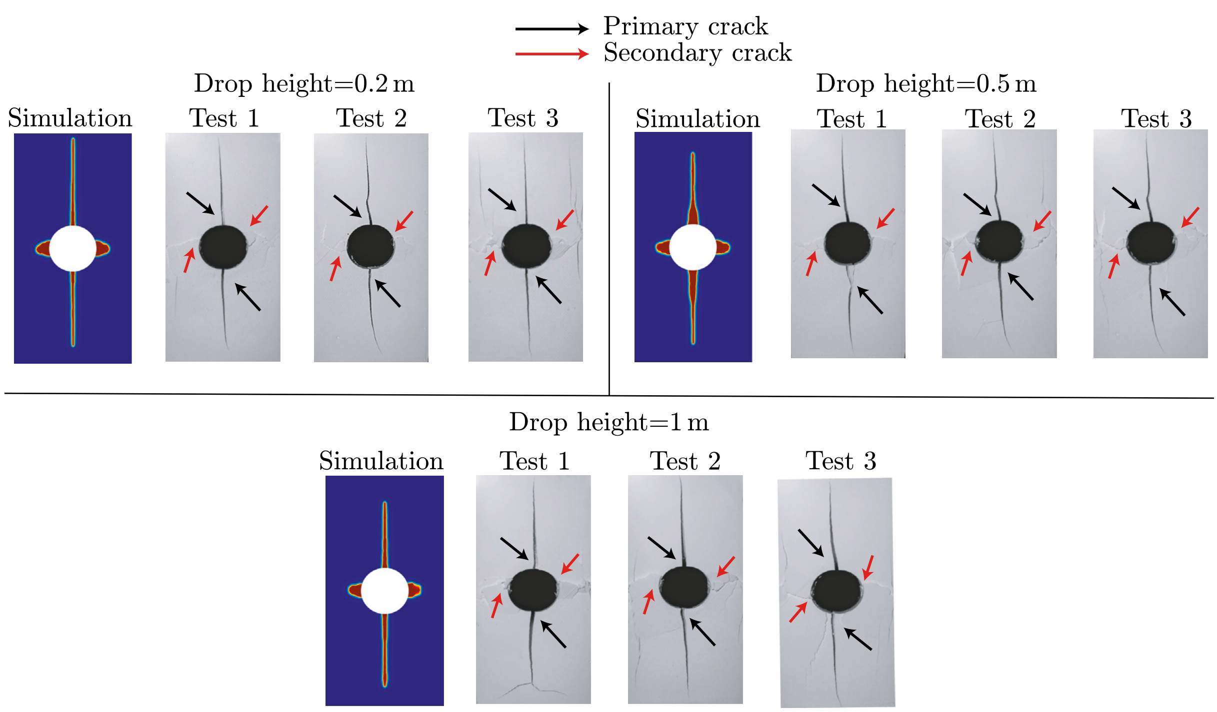

Fig. 10. Single-hole: Crack paths for simulations and experiments for different heights.

gypsum plaster used in the experiments. The material contains pores and microstructural irregularities that are not explicitly represented in the numerical simulations, which assume material homogeneity. In addition: friction effects between crack surfaces are neglected in the simulations but may appear in the experiments. These inherent complexities in the experimental material lead to variations in crack curvature, length, and inclination, which are challenging to reproduce numerically. Despite these challenges, the simulations capture the primary trends and mechanisms observed in the experiments, including the formation of tensile cracks followed by compressive cracks, interpreted as crushing.

A particularly important development in recent phase-field fracture modeling is the explicit incorporation of material strength, in addition to elasticity and fracture energy (Kumar et al., 2020, 2022; Larsen et al., 2024; Lopez-Pamies et al., 2025; Kamarei et al., 2025). As described by Lopez-Pamies et al. (2025), this is achieved by introducing a strength-based driving force directly into the evolution equation, enabling crack nucleation to be governed by a predefined strength surface under general stress states. These models depart from classical variational approaches and provide enhanced predictive capabilities, particularly for nucleation-dominated problems. In contrast, the present model remains within the energy-based phase-field framework, and introduces strength implicitly through a linear Mohr failure criterion that activates degradation under compression. This model recovers the classical hydrostatic-deviatoric formulation in tension, engages the Mohr criterion in compression, and blends the two in mixed-mode scenarios. Other failure criteria such as Drucker–Prager (Drucker and Prager, 1952) or nonlinear Mohr fracture surfaces can also be employed depending on the material or application. The effectiveness of current approach has been demonstrated in a former work (Hesammokri et al., 2023), where it successfully reproduced crack initiation, propagation, and peak load in a Brazilian disk test. While the model is energetic in nature, the incorporation of this failure envelope provides sufficient predictive capability for the dynamic fracture problems addressed here. However, a promising direction for future work is to incorporate explicit strength criteria into the evolution law to improve the model's

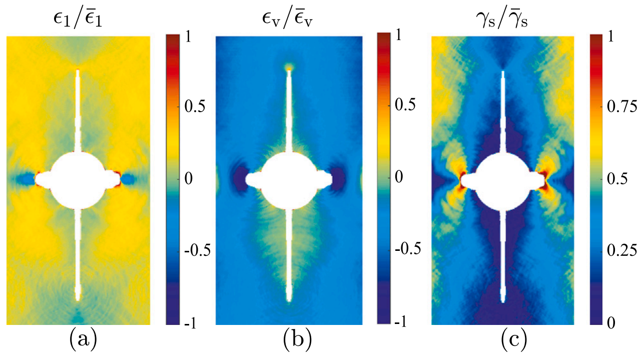

Fig. 11. Single-hole simulation: Distributions of first principal strain ϵ_1 (a), volumetric strain ϵ_v (b), and principal shear strain γ_s (c). The strain fields are normalized by their highest values, $\bar{\epsilon}_1$, $\bar{\epsilon}_v$ and $\bar{\gamma}_s$, respectively.

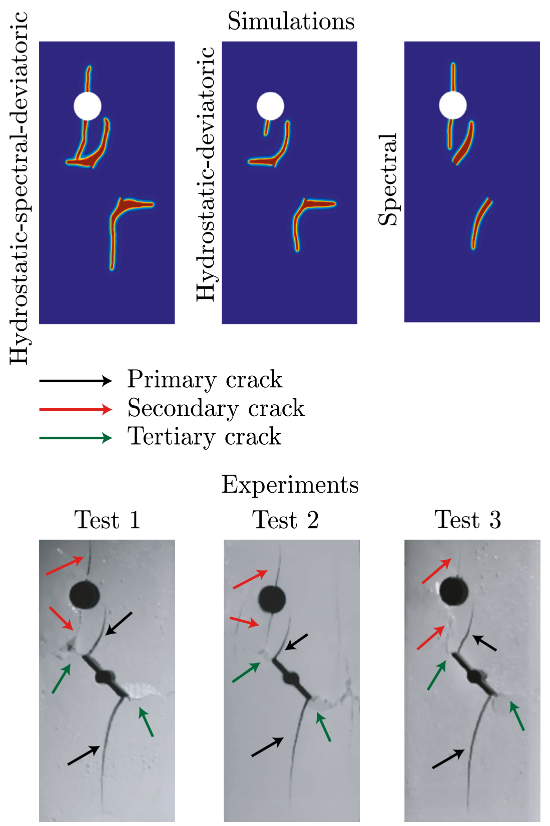

Fig. 12. Inclined notch with one hole: Crack paths for simulation and experiments for $h_{\text{drop}} = 0.2$ m.

predictive capability in general crack nucleation scenarios. As a final remark, an interesting aspect to consider is using adaptive mesh refinement (AMR) techniques, which dynamically concentrate resolution in regions of evolving damage. This approach offers promising potential to improve computational efficiency and scalability, particularly for larger or more complex fracture simulations.

6. Conclusions

Dynamic fracture processes in brittle materials are complex, particularly under mixed-mode compressive loading scenarios. To accurately simulate these phenomena, a hydrostatic-spectral-deviatoric decomposition was implemented in dynamic finite element models using a unified set of material parameters. This approach, which effectively splits assumed tensile and compressive strain contributions, addresses the limitations of traditional models in capturing crack evolution under compressive stresses. By incorporating distinct critical energy release rates for different fracture modes, the model achieves a higher degree of accuracy in predicting fracture evolution. Validation was achieved through dynamic experiments, including drop tower tests on brittle gypsum plaster specimens with embedded flaws and holes, with a high-speed camera monitoring crack propagation. Numerical simulations closely mirrored the experimental results, successfully reproducing primary, secondary, and tertiary crack paths as well as indicated a sound crack tip velocity. The model's ability to predict crack paths was evaluated against two well-established decomposition methods in the field (hydrostatic-deviatoric and spectral) and the results illustrate that the hydrostatic-spectral-deviatoric decomposition outperforms the two other decomposition methods. Based on the results, the hydrostatic-spectral-deviatoric decomposition offers profound insights into fracture mechanisms and proves highly effective in dynamic simulations for accurately predicting crack paths and other key fracture aspects.

CRediT authorship contribution statement

P. Hesammokri: Writing – review & editing, Writing – original draft, Visualization, Validation, Methodology, Investigation, Formal analysis, Data curation, Conceptualization. **S. Ershadrad:** Investigation. **P. Isaksson:** Writing – review & editing, Validation, Supervision, Software, Resources, Project administration, Methodology, Investigation, Funding acquisition, Formal analysis, Data curation, Conceptualization.

Declaration of competing interest

The authors declare that they have no known competing financial interests or personal relationships that could have appeared to influence the work reported in this paper.

Acknowledgments

The authors would like to acknowledge the Swedish Energy Agency, Sweden for the financial support [project P2023-00073].

Appendix A

To evaluate the feasibility of the hydrostatic-spectral-deviatoric decomposition in dynamic scenarios, it is applied to simulate two well-known dynamic crack growth cases. Simulations employing the hydrostatic-spectral-deviatoric decomposition are further contrasted to simulations using the spectral decomposition, which often has been used in simulations of these dynamic problems, cf. Borden et al. (2012). To allow for fair comparisons, an infinite cohesive strength is assumed (i.e., $c \to \infty$), hence, material crushing is disregarded. Energy can only dissipate as surface energy by fracture, $\Pi_s = W - \Pi_k - \Pi_e$, where W is the work done by external load, Π_k is the kinetic energy and Π_e is the stored elastic strain (or, potential) energy. Plane deformation is assumed to prevail.

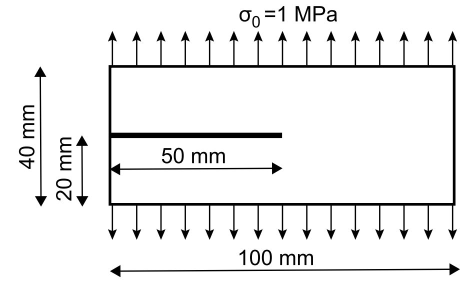

Fig. A.1. Geometry and boundary conditions.

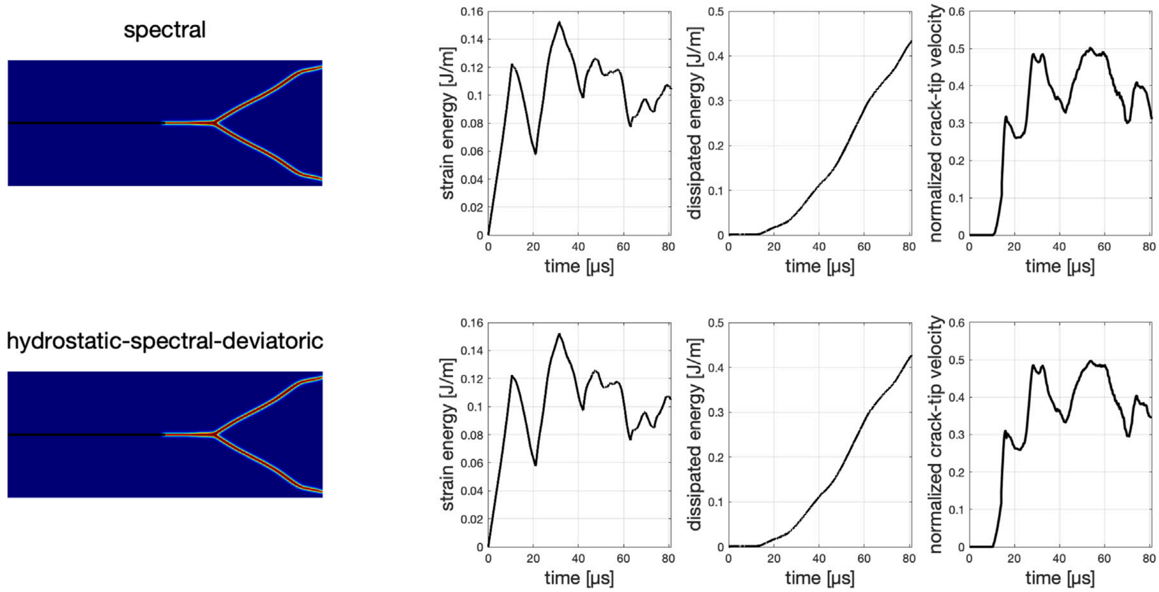

Fig. A.2. Dynamic crack branching: Comparison between the spectral decomposition (upper row) and the hydrostatic-spectral-deviatoric decomposition (lower row).

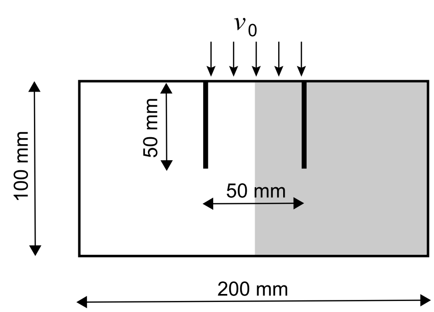

Fig. A.3. Geometry and boundary conditions. Symmetry is indicated by a gray region.

A.1. Dynamic crack branching

A pre-cracked rectangular body is loaded in tension, Fig. A.1. This problem has been widely adopted to study dynamic crack branching. A uniform and constant tensile stress $\sigma_0 = 1$ MPa is applied along the top and bottom edges of the body. The material parameters are: density $\rho = 2450$ kg/m^3, Young's modulus $E = 32$ GPa, Poisson's ratio $\nu = 0.2$, and energy release rates $G_{c\mathrm{I}} = G_{c\mathrm{II}} = 3$ N/m. The Rayleigh wave speed $c_R = 2120$ m/s, the internal length $l = 0.25$ mm and the element edge length $h = l/2$. The final fracture patterns for the two decompositions are shown in Fig. A.2, as well as plots showing evolving strain energy, dissipated energy and crack-tip velocity (normalized by the Rayleigh wave speed c_R) during the simulations. Dynamic crack branching occur in both models at about 36 μs and the crack-tip velocities never exceed the theoretical limit $0.6c_R$. The solutions have only sublime differences and are similar to the results in Borden et al. (2012).

A.2. Edge-cracked plate subject to impact load

The so-called Kalthoff-Winkler experiment, cf. Kalthoff and Winkler (1987), Kalthoff (2000), has been widely used to evaluate numerical models of failure under impact loadings. A pre-cracked specimen is impacted by a projectile, Fig. A.3. The material parameters are: density $\rho = 7850$ kg/m^3, Young's modulus $E = 190$ GPa, Poisson's ratio $\nu = 0.3$, and energy release rates $G_{c\mathrm{I}} = G_{c\mathrm{II}} = 22.1$ kN/m. The Rayleigh wave speed $c_R = 2826$ m/s, the internal length $l = 0.5$ mm and the element edge length $h = l/2$. The impact load is given by a constant uniform velocity $v_0 = 16.5$ m/s, Fig. A.3. For simplicity, symmetry is employed in the simulations. The final fracture patterns for the two decompositions are shown in Fig. A.4, as well as plots showing evolving strain energy, dissipated energy and crack-tip velocity (normalized by the Rayleigh wave speed c_R) during the simulations. The crack propagation angles are close to the experimentally observed angle of about 70°, cf. Kalthoff and Winkler (1987), Kalthoff (2000). As one may notice that the crack-tip velocities never exceed the theoretical limit $0.6c_R$. Also in this case, the solutions have only sublime differences and are similar to the results in Borden et al. (2012).

Appendix B

B.1. Fracture stress surface

Fig. B.1 display theoretical fracture stress surfaces in tension and compression, i.e. in-plane normal stress combinations to nucleate damage, when different decompositions are applied. Here, the stresses are normalized with σ_c, the theoretical uniaxial tensile stress nucleating damage in each decomposition. The applied material parameters are the same for all different decompositions and $G_{c\mathrm{I}} = G_{c\mathrm{II}}$ is adopted. In the case of the hydrostatic-spectral-deviatoric decomposition, the inherent cohesive stress c captures several values to reveal its influence.

To further illustrate the effective fracture strength predicted by the hydrostatic-spectral-deviatoric decomposition, the fracture stress surface is contrasted to a biaxial stress experiment on concrete found in literature (Guo, 2014). The experiment is reported to be almost in plane stress, i.e. one of the principal stresses is vanishing. The comparison demonstrates that the model reproduces the general shape and asymmetry of the measured fracture envelope, capturing the transition from tensile-dominated to compressive-dominated fracture.

Data availability

Data will be made available on request.

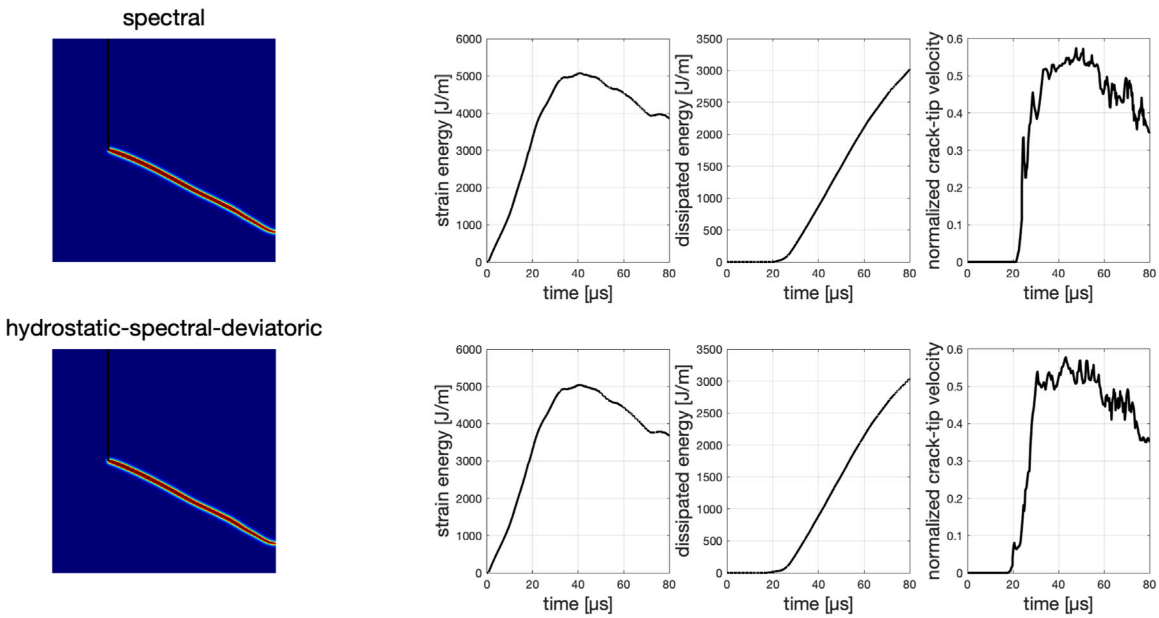

Fig. A.4. Edge-cracked plate subject to impact load: Comparison between the spectral decomposition (upper row) and the hydrostatic-spectral-deviatoric decomposition (lower row).

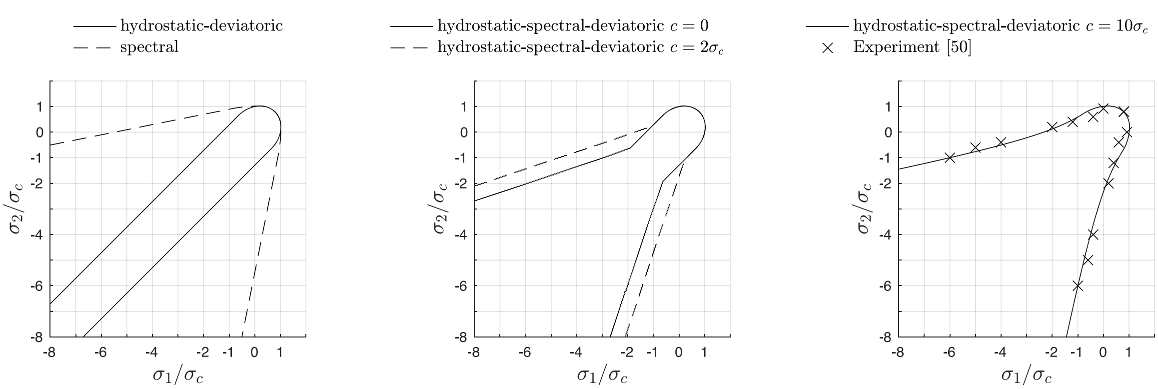

Fig. B.1. In-plane fracture stress surfaces given by the three different decomposition strategies. The hydrostatic-spectral-deviatoric decomposition using $c = 10\sigma_c$ is further contrasted to a reported biaxial fracture experiment on concrete (Guo, 2014). Note that the experimental stresses are here normalized differently than in Guo (2014).

References

Ambati, M., Gerasimov, T., De Lorenzis, L., 2015. A review on phase-field models of brittle fracture and a new fast hybrid formulation. Comput. Mech. 55 (2), 383–405.

Amor, H., Marigo, J.-J., Maurini, C., 2009. Regularized formulation of the variational brittle fracture with unilateral contact: Numerical experiments. J. Mech. Phys. Solid 57 (8), 1209–1229.

Bleyer, J., Alessi, R., 2018. Phase-field modeling of anisotropic brittle fracture including several damage mechanisms. Comput. Methods Appl. Mech. Engrg. 336, 213–236.

Borden, M.J., Verhoosel, C.V., Scott, M.A., Hughes, T.J., Landis, C.M., 2012. A phase-field description of dynamic brittle fracture. Comput. Methods Appl. Mech. Eng. 217, 77–95.

Bourdin, B., Francfort, G.A., Marigo, J.-J., 2000. Numerical experiments in revisited brittle fracture. J. Mech. Phys. Solid 48 (4), 797–826.

Braides, A., 1998. Approximation of Free-Discontinuity Problems. Springer.

Broberg, K.B., 1989. The near-tip field at high crack velocities. Struct. Integr. Theory Exp. 1–13.

Carlsson, J., Isaksson, P., 2018. Dynamic crack propagation in wood fibre composites analysed by high speed photography and a dynamic phase field model. Int. J. Solids Struct. 144, 78–85.

Carlsson, J., Isaksson, P., 2019. Crack dynamics and crack tip shielding in a material containing pores analysed by a phase field method. Eng. Fract. Mech. 206, 526–540.

Carollo, C., Davydov, D., Luding, S., Rumpf, M., 2020. Fracture in brittle materials under dynamic loading using phase-field modeling. Comput. Struct. 233, 106178.

Drucker, D.C., Prager, W., 1952. Soil mechanics and plastic analysis or limit design. Quart. Appl. Math. 10 (2), 157–165.

Francfort, G.A., Marigo, J.-J., 1998. Revisiting brittle fracture as an energy minimization problem. J. Mech. Phys. Solid 46 (8), 1319–1342.

Freund, L.B., Freud, L., 1998. Dynamic Fracture Mechanics. Cambridge Univ. Press.

Geelen, R.J., Liu, Y., Hu, T., Tupek, M.R., Dolbow, J.E., 2019. A phase-field formulation for dynamic cohesive fracture. Comput. Methods Appl. Mech. Engrg. 348, 680–711.

Guo, Z., 2014. Chapter 5 - multiaxial strength and constitutive relation. In: Guo, Z. (Ed.), Principles of Reinforced Concrete. Butterworth-Heinemann, Oxford, pp. 113–155.

He, J., Yu, T., Fang, W., Natarajan, S., 2024. Dynamic crack growth in orthotropic brittle materials using an adaptive phase-field modeling with variable-node elements. Comput. Struct. 337, 118068.

Hesammokri, P., Isaksson, P., 2024. Numerical analyses of brittle crack growth experiments in compression using a modified phase-field theory. Int. J. Solids Struct. 296, 112815.

Hesammokri, P., Yu, H., Isaksson, P., 2023. An extended hydrostatic–deviatoric strain energy density decomposition for phase-field fracture theories. Int. J. Solids Struct. 262, 112080.

Hofacker, M., Miehe, C., 2012. Continuum phase field modeling of dynamic fracture: variational principles and staggered FE implementation. Int. J. Fract. 178 (1), 113–129.

Kalthoff, J.F., 2000. Modes of dynamic shear failure in solids. Int. J. Fract. 101, 1–31.

Kalthoff, J.F., Winkler, S., 1987. Failure mode transition of high rates of shear loading. In: Chiema, C.Y., Kunze, H.D., Meyer, L.W. (Eds.), Proceedings of the International Conference on Impact Loading and Dynamic Behavior of Materials. pp. 185–195.

Kamarei, F., Dolbow, J.E., Lopez-Pamies, O., 2025. Nucleation of fracture: The first-octant evidence against classical variational phase-field models. J. Appl. Mech. 92 (1).

Kumar, A., Bourdin, B., Francfort, G.A., Lopez-Pamies, O., 2020. Revisiting nucleation in the phase-field approach to brittle fracture. J. Mech. Phys. Solids 142, 104027.

Kumar, A., Ravi-Chandar, K., Lopez-Pamies, O., 2022. The revisited phase-field approach to brittle fracture: application to indentation and notch problems. Int. J. Fract. 237 (1), 83–100.

Labuz, J.F., Zang, A., 2012. Mohr–Coulomb failure criterion. Rock Mech. Rock Eng. 45 (6), 975–979.

Larsen, C.J., 2010. Models for dynamic fracture based on Griffith's criterion. In: IUTAM Symposium on Variational Concepts with Applications to the Mechanics of Materials: Proceedings of the IUTAM Symposium on Variational Concepts with Applications to the Mechanics of Materials, Bochum, Germany, September 22–26, 2008. Springer, pp. 131–140.

Larsen, C., Dolbow, J.E., Lopez-Pamies, O., 2024. A variational formulation of griffith phase-field fracture with material strength. Int. J. Fract. 247 (3), 319–327.

Li, V.C., 1986. Mechanics of Shear Rupture Applied to Earthquake Zones. Tech. Rep.

Li, W., Nguyen-Thanh, N., Du, H., Zhou, K., 2023. Adaptive phase-field modeling of dynamic brittle fracture in composite materials. Compos. Struct. 306, 116589.

Lopez-Pamies, O., Dolbow, J.E., Francfort, G.A., Larsen, C.J., 2025. Classical variational phase-field models cannot predict fracture nucleation. Comput. Methods Appl. Mech. Engrg. 433, 117520.

Mandal, T.K., Nguyen, V.P., Wu, J.-Y., 2020. Evaluation of variational phase-field models for dynamic brittle fracture. Eng. Fract. Mech. 235, 107169.

MATLAB, 2024. R2024a. The MathWorks Inc., Natick, Massachusetts.

Mehrmashhadi, J., Bahadori, M., Bobaru, F., 2020. On validating peridynamic models and a phase-field model for dynamic brittle fracture in glass. Eng. Fract. Mech. 240, 107355.

Miehe, C., Hofacker, M., Welschinger, F., 2010a. A phase field model for rate-independent crack propagation: Robust algorithmic implementation based on operator splits. Comput. Methods Appl. Mech. Eng. 199 (45–48), 2765–2778.

Miehe, C., Welschinger, F., Hofacker, M., 2010b. Thermodynamically consistent phase-field models of fracture: Variational principles and multi-field FE implementations. Internat. J. Numer. Methods Engrg. 83 (10), 1273–1311.

Nejati, M., Bahrami, B., Ayatollahi, M.R., Driesner, T., 2021. On the anisotropy of shear fracture toughness in rocks. Theor. Appl. Fract. Mech. 113, 102946.

Newmark, N.M., 1959. A method of computation for structural dynamics. J. Eng. Mech. Div. 85 (3), 67–94.

Nguyen, T.T., Yvonnet, J., Zhu, Q.-Z., Bornert, M., Chateau, C., 2015. A phase field method to simulate crack nucleation and propagation in strongly heterogeneous materials from direct imaging of their microstructure. Eng. Fract. Mech. 139, 18–39.

Pham, K., Amor, H., Marigo, J.-J., Maurini, C., 2011. Gradient damage models and their use to approximate brittle fracture. Int. J. Damage Mech. 20 (4), 618–652.

Rosakis, A., Samudrala, O., Coker, D., 1999. Cracks faster than the shear wave speed. Science 284 (5418), 1337–1340.

Schlüter, A., Kuhn, C., Müller, R., Gross, D., 2016. An investigation of intersonic fracture using a phase field model. Arch. Appl. Mech. 86 (1), 321–333.

Shajan, A.M., Piska, R., Natarajan, S., 2023. Study of mixed-mode fracture in functionally graded material using an adaptive phase-field fracture model. Compos. Struct. 117708.

Shen, B., Stephansson, O., 1994. Modification of the G-criterion for crack propagation subjected to compression. Eng. Fract. Mech. 177–189.

Spetz, A., Denzer, R., Tudisco, E., Dahlblom, O., 2020. Phase-field fracture modelling of crack nucleation and propagation in porous rock. Int. J. Fract. 224 (1), 31–46.

Spetz, A., Denzer, R., Tudisco, E., Dahlblom, O., 2021. A modified phase-field fracture model for simulation of mixed mode brittle fractures and compressive cracks in porous rock. Rock Mech. Rock Eng. 54 (10), 5375–5388.

Suh, H.S., Sun, W., O'Connor, D.T., 2020. A phase field model for cohesive fracture in micropolar continua. Comput. Methods Appl. Mech. Engrg. 369, 113181.

Tanné, E., Li, T., Bourdin, B., Marigo, J.-J., Maurini, C., 2018. Crack nucleation in variational phase-field models of brittle fracture. J. Mech. Phys. Solids 110, 80–99.

Wu, J.-Y., Nguyen, V.P., 2018. A length scale insensitive phase-field damage model for brittle fracture. J. Mech. Phys. Solids 119, 20–42.

Yi, D., Yang, Z., Yi, L., Liu, J., Gou, L., Peng, Q., Zheng, N., Li, X., 2025. Simulation of dynamic pulse fracturing in elastoplastic media based on a mixed-mode fatigue phase-field model. Comput. Geotech. 179, 107043.

Zhang, X., Sloan, S.W., Vignes, C., Sheng, D., 2017. A modification of the phase-field model for mixed mode crack propagation in rock-like materials. Comput. Methods Appl. Mech. Eng. 322, 123–136.